Results in Physics 22 (2021) 103847

Contents lists available at ScienceDirect

Results in Physics

journal homepage: www.elsevier.com/locate/rinp

Laser micromachining of steel and copper using femtosecond laser pulses in GHz burst mode

Ona Balachninaitė *, Viktorija Tamulienė, Laurynas Eičas, Virgilijus Vaičaitis

Laser Research Center, Vilnius University, Sauletekio ave. 10, Vilnius LT 10223, Lithuania

ARTICLE INFO

Keywords:
Ultra-short laser pulses
GHz burst mode
Metal ablation
Plasma shielding
Micromachining

ABSTRACT

Investigations on the ablation of steel and copper with femtosecond laser pulses using single pulses and bursts of infinite sequence of pulses with 1 GHz intraburst repetition rate are presented in this paper. The ablation efficiency is compared to the case of single femtosecond laser pulses. Based on the literature a model of the ablation process is presented explaining the behavior of a pulse burst and the good qualitative agreement of the numerical and experimental ablation efficiencies is obtained.

1. Introduction

Ultrashort pulsed lasers are playing an increasingly important role in many industrial manufacturing processes due to their ability for high-quality material processing for many different materials, high precision and flexibility [1,2]. However, in a competitive industry, machining productivity must always grow and the demand for high throughput still remains one of the important factors. In recent years, the burst-mode regime was widely investigated in ultrashort-pulse laser micromachining. The use of bursts of two [3–5] and several [6–11] ultra-short pulses for micromachining of metals as well as the impact of the burst mode on ablation efficiency has been widely investigated. It was showed that laser processing with 2–3 burst pulses at intra-burst frequencies close to 80 MHz may lead to varying ablation efficiencies for the individual intra-burst pulses, which could be explained by shielding and material re-deposition processes induced by the second pulse of a burst [12]. In [13] article it was found that the ablation efficiency ratio between femtosecond single-pulse mode and burst mode strongly depends on the material. It was demonstrated that the fs-laser in 28-pulse-burst mode at 148MHz frequency generates similar features (burr and droplets) as the nanosecond laser when processing at the optimum efficiency. The femtosecond laser in burst mode achieved about 2/3 of the nanosecond laser efficiency regardless of the material. This correlation in ablation efficiency and quality indicates that the underlying ablation physics of a burst-mode laser emitting 28 burst pulses at 148 MHz frequency is different from single pulse and it could be related to the nanosecond pulse ablation. The reported [10] copper ablation experiments with up to 800 burst pulses and frequencies up to 3.46 GHz showed that at the optimal experimental parameters (the number of pulses in the burst more than 25 and intra-burst frequency more than 108 MHz) the ablation efficiency may increase significantly due to ablation-cooled material removal. However, [11] showed that this increase of ablation efficiency is only observable for percussion drilling. Potentially significant high increase of ablation efficiency using high number of subpulses in burst trains of pulses with the GHz repetition rate has been shown in several recent works [14–16]. On the contrary, [17] demonstrated the tremendous reduction of the specific removal rate in metals for surface texturing by using burst trains of pulses with the GHz repetition rate. In recently reported [18] it was demonstrated that the burst duration and number of pulses in the burst are the main parameters of fs GHz processing and on choosing optimal parameters not only an optimal ablation efficiency can be achieved but also the thermal effects can be controlled.

In this context, the goal of the presented study was to investigate the advantages or disadvantages of the burst mode regime by comparing it with the single-pulse regime. We determined ablation efficiencies as a function of fluence for stainless steel and copper and compared the ablation parameters at the optimal fluence using the femtosecond laser operated in single-pulse mode and in burst mode of 1 GHz pulse frequency. A femtosecond laser and beam splitter mirrors were used to obtain pulse-bursts, that a single pulse was divided into infinite sequence of the pulses and the energy of the single pulse was kept equal to the integrated energy of the pulses in the burst. The energy distribution of the pulses in the burst could be controlled by choosing different beamsplitters. Moreover, the theoretical model for the burst ablation is presented. It is based on [19] where the two temperature model for the axial-symmetric model was described.

* Corresponding author.
E-mail address: ona.balachninaite@ff.vu.lt (O. Balachninaitė).

https://doi.org/10.1016/j.rinp.2021.103847
Received 30 October 2020; Received in revised form 11 December 2020; Accepted 12 January 2021
Available online 19 January 2021

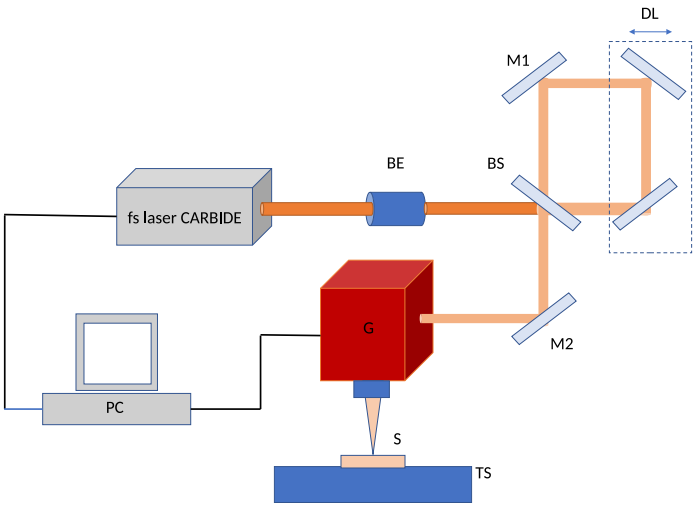

Fig. 1. Experimental setup of laser processing system in femtosecond burst mode. Optical components include beamsplitter (BS), mirror (M), beam expander (BE), G — galvanoscanner, DL — delay line for the burst pulse mode formation, TS — translation stage, S — sample.

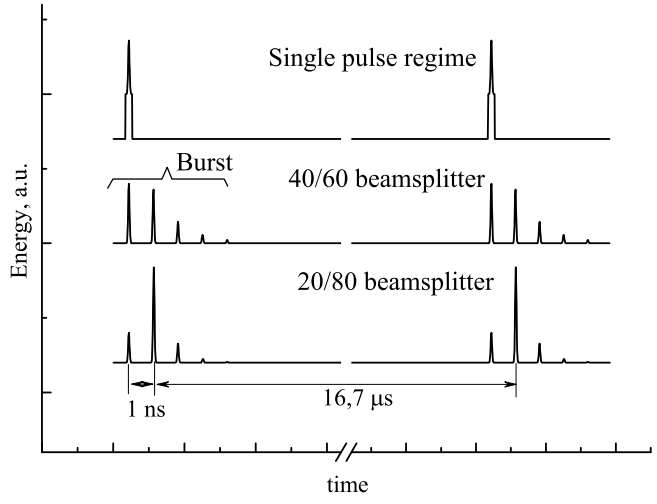

Fig. 2. Single-pulse (top) and burst (middle and bottom) regimes used in the experiment.

2. Experiment

2.1. Experimental setup

A schematic representation of the experimental setup is shown in Fig. 1. The experiments were performed using the Carbide® Yb:KGW femtosecond laser system (Light Conversion Ltd) operating at 1030 nm (pulse width 280 fs, average power up to 5 W, 60 kHz). The maximum laser energy of a single femtosecond pulse was approximately 80 μJ.

The burst of multiple pulses was formed by dividing the beam with the beam splitter BS, which transmitted one part and reflected another part of the incident laser wavelength (1030 nm). The transmitted part of the laser radiation, undergoing multiple reflections by high reflective (99,95%) dielectric multi-layer mirrors M1–M2, formed a sequence of endless multiple pulses with decreasing energy (Fig. 2). Two different beamsplitters (EKSMA Optics Ltd.) were used in the experiment. One beam splitter transmitted 80% and reflected 20% of the incident laser light and another one transmitted 60% and reflected 40% of the incident laser light. Thus, for the first beam splitter, if the energy of the primary single pulse was 80 μJ, the energies of the multiple pulses in the sequence were 24 μJ; 39.2 μJ; 11.8 μJ; 3.5 μJ etc., respectively. Actually, the first two-three burst pulses were the most significant at our experimental conditions because at low fluences the energies of 4th, 5th etc. separate pulses in the burst were below the ablation threshold. For the theoretical consideration only the first three pulses were taken into account, but it should be kept in mind that at higher fluence values, far from the ablation threshold, the 4th and even the 5th pulses could influence the ablated volume. The delay between the pulses in the burst was kept constant and equal to 1 ns. The experiments were carried out applying linearly parallel-polarized pulses in the burst. Then, collinearly propagating beams were positioned using a dual-axis galvanometric scanner (ScanLab Inc.). The galvanometer includes two ultra-light dielectric motor-control mirrors. The motors move the mirrors synchronizing with laser pulses and an image could be produced on the surface of the sample, using the control software SCA (Altechna, UAB). The typical scan angle of the galvanometer is ±0.35 rad, and the diameter of the aperture is 10 mm, the maximum marking speed is 3.5 m/s and the positioning speed is 12 m/s. The system is also entirely accurate, and its repeatability is <2 μrad, and the deviation error is low – 0.11 m/s.

After the laser beam passed through the scanner, it was focused by an F-theta lens (f = 75 mm) in the normal incidence onto the sample, which was mounted on a three-dimensional motorized positioning stage (Standa Inc.) for precise positioning of the sample at the start. Micromachining was carried out on copper and steel samples.

The table could be controlled by the software (SMCVieW) that can be synchronized with the SCA application. Galvanometric scanners in combination with F-theta lenses can produce large scanning fields and scanning rates of the order of m/s or greater.

The optical profilometer Plμ 2300 (Sensofar) with the resolution of 0.1 nm, characteristic of a fast-confocal scanning (12.5 confocal images per second) and a vertical scanning rate of 800 μm/s was used to observe the formed grooves in the experiments. The electronic microscope TM-1000 (Hitachi) was used to estimate the surface structure of the grooves and the amount of substance removed near the groove. The device is able to scan and magnify the image up to 10,000X.

2.2. Experimental results

During the experiment, the ablation efficiency of steel and copper samples was investigated using single pulses emitted by the femtosecond laser and the burst mode pulses formed with the delay line. All experiments were performed on 4 mm-thick stainless steel AISI 316L and 2 mm-thick unpolished copper DHP (C12 200-99,9%) samples.

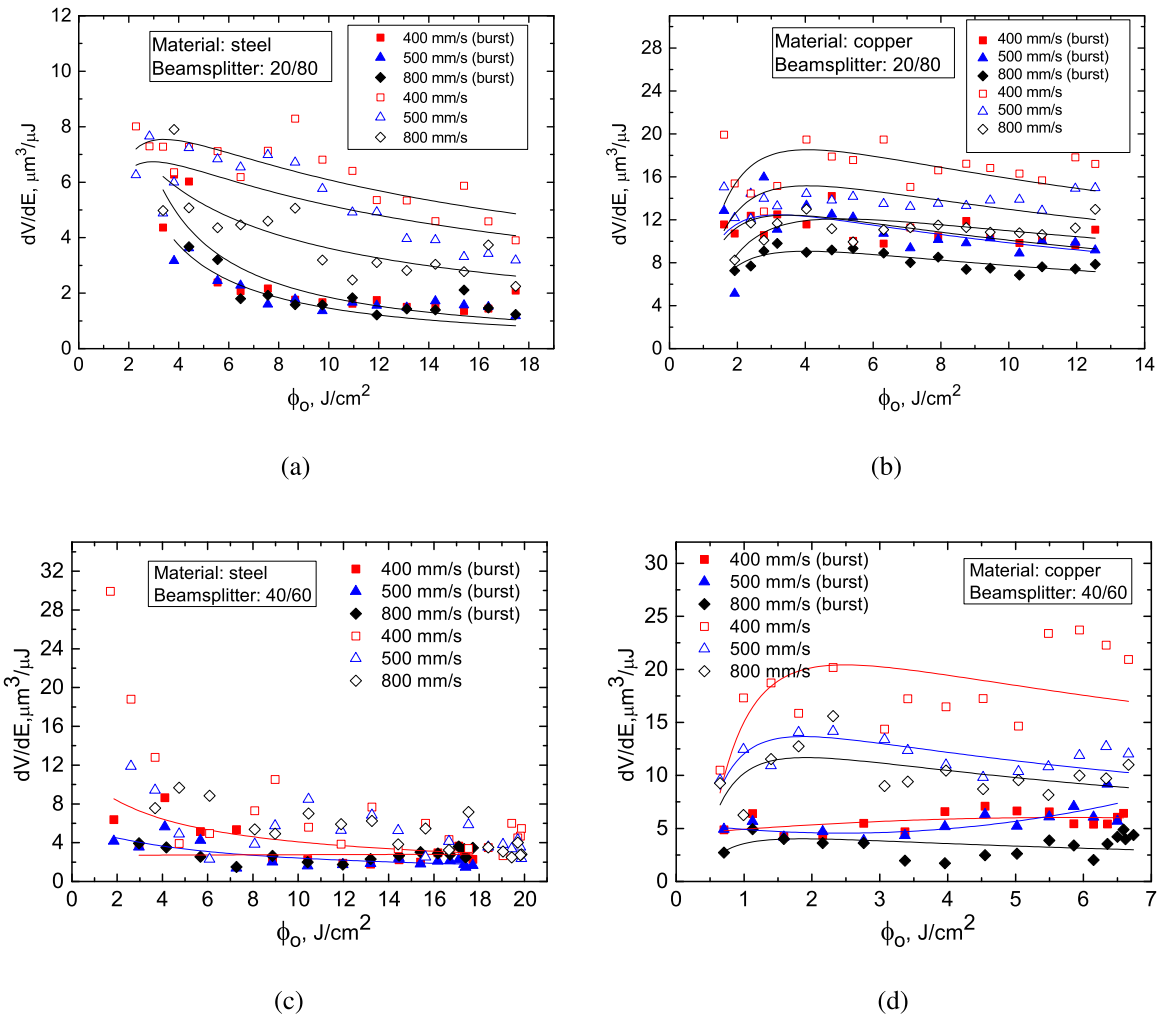

Fig. 3. Ablation efficiency versus peak pulse fluence for a steel (a, c) and copper (b, d) at various beam scanning speeds for beamsplitters 20/80 (a, b) and 40/60 (c, d). Solid symbols represents the burst mode, open-the single pulse mode. The lines are guides to the eye.

The tests were conducted at room temperature under normal ambient pressure. No additional cleaning of the samples before the laser processing was applied. The laser beam moved on the sample surface using the galvanometer IntelliSCAN. The image programmed in the SCA application was reproduced on the surface of the sample: 3 mm long lines with the spacing of 0.5 mm. Each line was passed with the laser beam 20 times, and each line was formed at different scanning speeds of 400, 500 and 800 mm/s. Laser pulse repetition rate was fixed and equal to 60 kHz. The measurements were repeated continuously changing laser average output power from 0.4 W to 3.2 W. The grooves were formed by a single mode and the burst pulse mode. The burst mode was realized by using two different beamsplitters: 40/60 and 20/80. The optical profilometer was used to measure the depth and width of the grooves. The laser beam radius and the ablation threshold flow value for experiments with both samples were experimentally determined using single pulses. Knowing these values, it was also possible to determine the optimum radiative flux for the most efficient removal of the substance in the case of a single-pulse regime. To determine the threshold of the laser ablation ϕ_{th} and the laser beam radius ω_0, the Liu approach was applied [20]. The focusing conditions for experiments with steel and copper samples were slightly different. The estimated laser beam radius for experiment with the steel sample was 13.9 ± 1.4 μm, and the laser beam radius used for the experiment with the copper sample was 16.5 ± 0.6 μm. The estimated threshold of the laser ablation was 0.28 ± 0.05 J/cm^2 and 0.51 ± 0.08 J/cm^2 for steel and copper respectively, which corresponds to the values in the literature (steel- [21], copper- [22]). In order to compare the ablation efficiency the optimal fluence was calculated according to the [8]. The optimal fluence was 2.1 ± 0.4 J/cm^2 and 3.8 ± 0.6 J/cm^2 for steel and copper respectively.

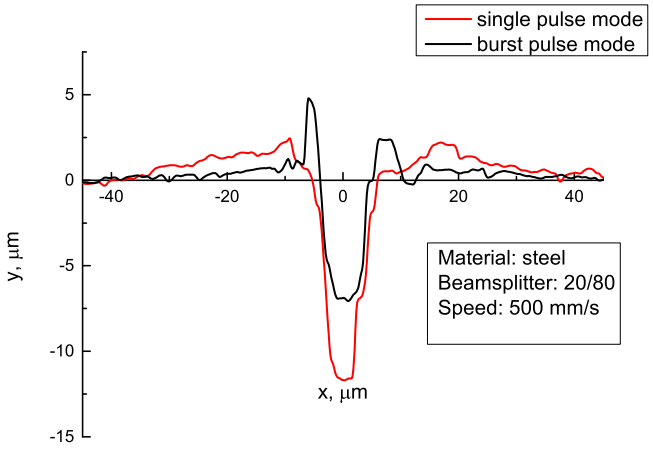

Fig. 4. Crater profiles of femtosecond ablation on the steel sample obtained with single pulse and burst pulses.

Based on Two-Temperature Model where the ablation depth logarithmically depends on the applied fluence the specific removal rate per average power (assumed that the beam profile is Gaussian) dV/dE can be calculated as follows [6]:

$$\frac{dV}{dE} = \frac{dV}{dt}\frac{1}{P_{av}} = \frac{\delta}{2}\frac{1}{\phi_0}\ln^2(\phi_0/\phi_{th}), \tag{1}$$

where V is the volume; dV/dE is the ablation rate per average power; δ is energy penetration depth, ϕ_{th} is the threshold fluence, P_{av} denotes average laser output power, ϕ_0 is the peak fluence (in the center of the Gaussian beam). The peak fluence can be estimated by Kleinert et al. [11]:

$$\phi_0 = \frac{2E_p}{\pi\omega_0^2} \tag{2}$$

where Ep is the pulse energy, ω_0 is laser beam diameter at $1/e^2$. The removed volume per pulse energy can be rewritten (Neuenschwander):

$$\frac{dV}{dE} = \frac{\Delta V}{E_p} = \frac{hp^2}{N_{scan}}\frac{f_p}{P_{av}} = \frac{hp^2}{N_{scan}}\frac{1}{E_p} \tag{3}$$

where N_{scan} is the number of laser beam scans, h and p are the depth and the width of the ablated grooves, respectively. Ablation efficiency at single and burst-regimes was evaluated for copper and steel respectively. For the calculation of the volume of the groove ablated by single pulse the paraboloid approximation was used. Fig. 3 shows the specific material removal rate in dependence on the fluence for steel and copper using single pulse and burst-mode regimes. The specific material removal rate decreased by increasing the laser fluence and the scanning speed. The same tendency was observed for different energy distribution between the pulses (for 40/60 and 20/80 beamsplitters) in the burst and for different materials. For the burst mode this decrease in the material removal rate could be caused by the formation of the debris (Fig. 4), which started to appear at the energy density more than twice above the optimal energy density value. The observed up to 10 μm debris formation during laser ablation by burst pulses could be explained by an increased melt ejection. A part of the irradiated material was melted and displaced instead of being evaporated. Similar material re-deposition effects were reported in [12,18]. No decolorisation areas of the samples or heat affected zones were observed. At the optimal laser energy density (2 J/cm^2) the ablation efficiency using burst mode regime decreased the most and was 65%–75% lower in comparison to the single pulse regime. It could be caused by plasma shielding effect: the cloud of the particles formed after the first laser pulse and plasma above the groove started to shield the next pulses and these pulses are not involved in the ablation process [23]. At the optimal energy fluence value specific material removal rate in a single pulse regime was 25%–35% higher than in the case of burst mode regime. The specific removal rate follows the same function for bursts and single pulses. With the 40/60 beamsplitter which corresponds to energy distribution between the pulses in the burst equal to 1:3.2:0.64:0,128.. etc., the higher specific removal rate could be achieved in comparison to the case when energy distribution between the pulses in the burst is 1:0.9:0.36:0.144... etc. Although, a higher specific removal rate was not achieved using bursts, compared to the single pulses, we managed to observe few configurations where the margins are modest. The highest efficiency using 1:3.2:0.64:0.128..sequence and <2 J/cm^2 energy density was obtained, therefore for steel the removal was 15% and for copper only 5% lower compared to the grooves ablated with the single pulses. Depth-to-width ratio of the processed grooves were measured for single and burst mode regimes in dependence on the laser beam scanning speed (Fig. 5). In single pulse regime as in burst pulse regime, the aspect ratio of the groove decreases by increasing the scanning speed. The width of the grooves remains almost constant for different scanning speeds, while the depth of the grooves decreases with the increase of the scanning speed. This is because the laser energy accumulated in unit area of the samples decreases with the increase of the scanning speed, which makes the ablation efficiency of samples decrease, consequently the depth of the grooves decreases. However, higher aspect-ratio grooves were produced by burst of tightly focused femtosecond laser pulses in comparison to single pulse regime. The narrower grooves were processed by using burst of the pulses.

3. Numerical modeling

In this Section, we simulate the heat equations when the metal is ablated by (1) a single pulse; (2) pulses' burst formed by a 20/80 beamsplitter; (3) pulses' burst formed by a 40/60 beam splitter. In the cases (2) and (3) three first pulses are taken as input. As in the experiment, pump wavelength $\lambda = 1030$ nm, pulse duration $t_p = 290$ fs, duration between pulses $\tau = 1$ ns. Beam radius at $1/e^2$ level $r_D = 17$ μm.

3.1. Governing equations

Here, we implement the axisymmetric two-temperature model that describes the evolution of electron and lattice temperatures T_e and T_l as well as heat fluxes of electrons and lattice $\mathbf{q}_e$ and $\mathbf{q}_l$. The equations read [19]:

$$\begin{aligned}
C_e(T_e)\frac{\partial T_e}{\partial t} &= -\nabla\cdot\mathbf{q}_e - G(T_e,T_l)(T_e-T_l) \\
&\quad + Q(r,z,t), \\
C_l\frac{\partial T_l}{\partial t} &= -\nabla\cdot\mathbf{q}_l + G(T_e,T_l)(T_e-T_l), \\
T_l &\neq T_m,\ T_l \neq T_b, \\
\mathbf{q}_e + \tau_e\frac{\partial \mathbf{q}_e}{\partial t} &= -\lambda(T_e,T_l)\nabla T_e, \\
\mathbf{q}_l + \tau_l\frac{\partial \mathbf{q}_l}{\partial t} &= -\lambda_l\nabla T_l,
\end{aligned} \tag{4}$$

$$\begin{aligned}
\int_{t_{mb}}^{t_{me}}[-\nabla\cdot\mathbf{q}_l + G(T_e,T_l)(T_e-T_l)]dt &= Q_m, \\
T_l &= T_m,
\end{aligned} \tag{5}$$

$$\begin{aligned}
\int_{t_{bb}}^{t_{be}}[-\nabla\cdot\mathbf{q}_l + G(T_e,T_l)(T_e-T_l)]dt &= Q_{ev}, \\
T_l &= T_b,
\end{aligned}$$

where Q is the laser irradiation source term:

$$\begin{aligned}
Q = &\sqrt{\frac{4\ln 2}{\pi}}(1-R) \\
&\times \sum_{j=0}^{N-1}\frac{\phi_{j0}}{\delta t_p}\exp\left[-\frac{r^2}{r_D^2} - \frac{z}{\delta}\right. \\
&\left. -4\ln 2\frac{(t-2t_p-j\tau)^2}{t_p^2}\right].
\end{aligned} \tag{6}$$

N is the amount of the pulses in the burst, τ is the duration between the jth and $(j+1)$th pulses. ϕ_{j0} is the fluence.

In Eqs. (5), Q_m and Q_{ev} are the volumetric latent heats of fusion and evaporation, respectively. T_m and T_b are the melting and boiling temperatures, respectively. These and other parameters will be described in details in Section 3.3.

3.2. Boundary conditions

We implement the same boundary and initial conditions as in [19]. At the boundary, $(r,z) \in \Gamma$ (no-flux condition):

$$\begin{aligned}
q_{be}(r,z,t) &= -\lambda_e(T_e,T_l)\left(\mathbf{n}\cdot\nabla T_e(r,z,t)\right) = 0, \\
q_{bl}(r,z,t) &= -\lambda_l\left(\mathbf{n}\cdot\nabla T_l(r,z,t)\right) = 0,
\end{aligned} \tag{7}$$

where $\mathbf{n}$ is the outward unit normal vector. When the material is removed due to the ablation, the boundary is modified.

Initial conditions at $t = 0$:

$$T_e(r,z,t) = T_l(r,z,t) = T_0. \tag{8}$$

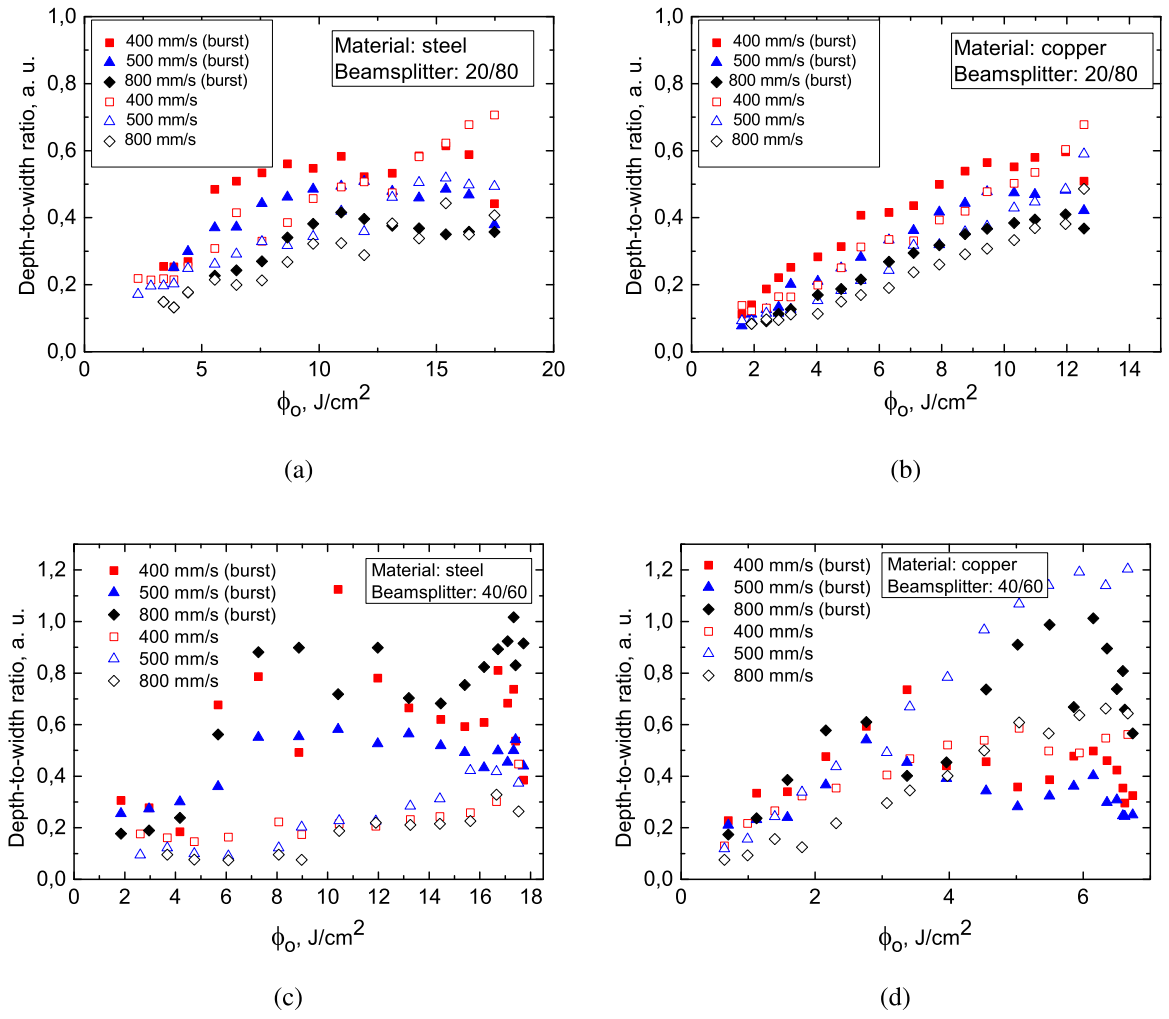

Fig. 5. Depth-to-width ratio versus peak pulse fluence for a steel (a, c) and copper (b, d) at various beam scanning speeds for beamsplitters 20/80 (a, b) and 40/60 (c, d). Solid symbols represent the burst mode, open-the single pulse mode.

3.3. Parameters' calculation

In this subsection we describe the calculation of steel and iron parameters.

Reflectance R and penetration depth δ: here we make use of the Drude model that gives the complex refractive index $n = n_r + in_i$, where $i = \sqrt{-1}$. The values of $n_r = 2.3$ and $n_i = 4.52$ were taken from [24], iron at 1 μm. Then, reflectance at the perpendicular incidence is given by $R = \frac{(n_r-1)^2+n_i^2}{(n_r+1)^2+n_i^2}$ and $R = 0.706$. Penetration depth is calculated from $\delta = \frac{1}{2}\frac{\lambda}{2\pi n_i}$, where $\lambda = 1.032$ μm. So, $\delta = 18.2$ nm.

Initial condition. In Eq. (8), $T_0 = 300$ K and it is constant.

Melting and boiling points. For iron, $T_m = 1811$ K and $T_b = 3134$ K.

Volumetric latent heat of fusion Q_m. For iron, $Q_m = \frac{13.8\ \text{kJ/mol}}{55.845\ \text{g/mol}} \times 7.874\ \text{g/cm}^3 = 1946\ \text{MJ/m}^3$.

Volumetric latent heat of evaporation Q_{ev}. For iron, $Q_{ev} = \frac{340\ \text{kJ/mol}}{55.845\ \text{g/mol}} \times 7.874\ \text{g/cm}^3 = 47939\ \text{MJ/m}^3$.

Volumetric specific heats $C_e(T_e)$ and C_l.

$C_l = 0.45\ \text{kJ/(kgK)} \times 7.84\ \text{g/cm}^3 = 3.53\ \text{MJ/(m}^3\ \text{K)}$.

Dependence $C_e(T_e)$ was taken from data of [25] (data for Fe-bcc). The data curve was approximated by a 6th-order polynomial function as it is shown in Fig. 6a. The obtained polynomial formula was implemented in the numerical simulation instead of the data file.

Thermal conductivities $\lambda_e(T_e, T_l)$ and λ_l.

$\lambda_l = \lambda_0 = 83.5$ W/(m K). In Drude model [19]

$$\lambda_e(T_e, T_l) = \frac{1}{3} C_e(T_e)\tau_e(T_e, T_l)v_e^2, \tag{9}$$

where $\tau_e(T_e, T_l)$ is the total electron scattering time and v_e is the mean velocity of the electrons. We take $v_e = v_F$, where v_F is the Fermi velocity.

Relaxation times τ_l and τ_e. Relaxation time of phonon collisions was taken the same as in gold: $\tau_l = 0.8$ ps. In Drude model, relaxation time of free electrons $\tau_e = m_e\sigma/(\rho e^2)$, where σ is the conductivity. m_e, e and ρ are the electron mass, charge and number density, respectively. At $\sigma = 10^7$ S/m, $\tau_e = 4.2$ fs. As τ_e is rather small, we set $\tau_e(T_e, T_l) = \tau_e$.

The electron–phonon coupling factor $G(T_e, T_l)$. In our model, $G(T_e, T_l) = G_e(T_e)$ and data for $G_e(T_e)$ was taken from [25]. Again, the approximation by a 6th order polynomial function was applied, Fig. 6b.

3.4. Numerical results

The governing Eqs. (5) were solved in the cylindrical coordinate system [19]. The single pulse as well as burst of pulses were simulated. Radial coordinate r and longitudinal coordinate z were described in the space intervals [0 50 μm] and [0 2 μm], respectively. The size of the matrix was 25 × 200. The time step was equal to 2.5 fs.

Single pulse was simulated from $t = 0$ to $t = 100$ ps and three pulses burst was simulated from $t = 0$ to $t = 2.1$ ns. The temperature profiles as well as the ablated craters at the fixed input fluence are

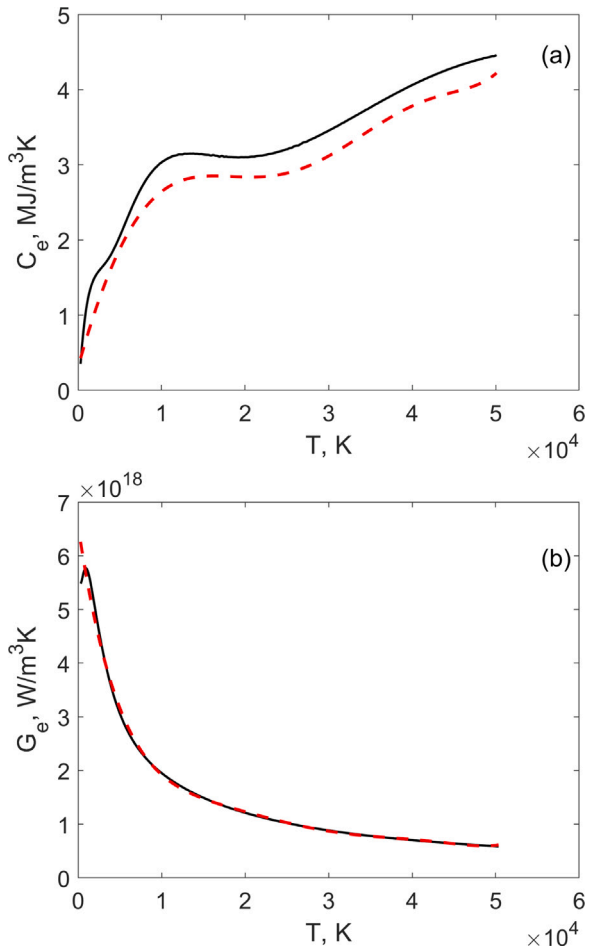

Fig. 6. Dependences of (a) $C_e(T_e)$ and (b) $G_e(T_e)$ from [25] data (black solid lines) and their 6th order polynomial fits (red dashed lines).

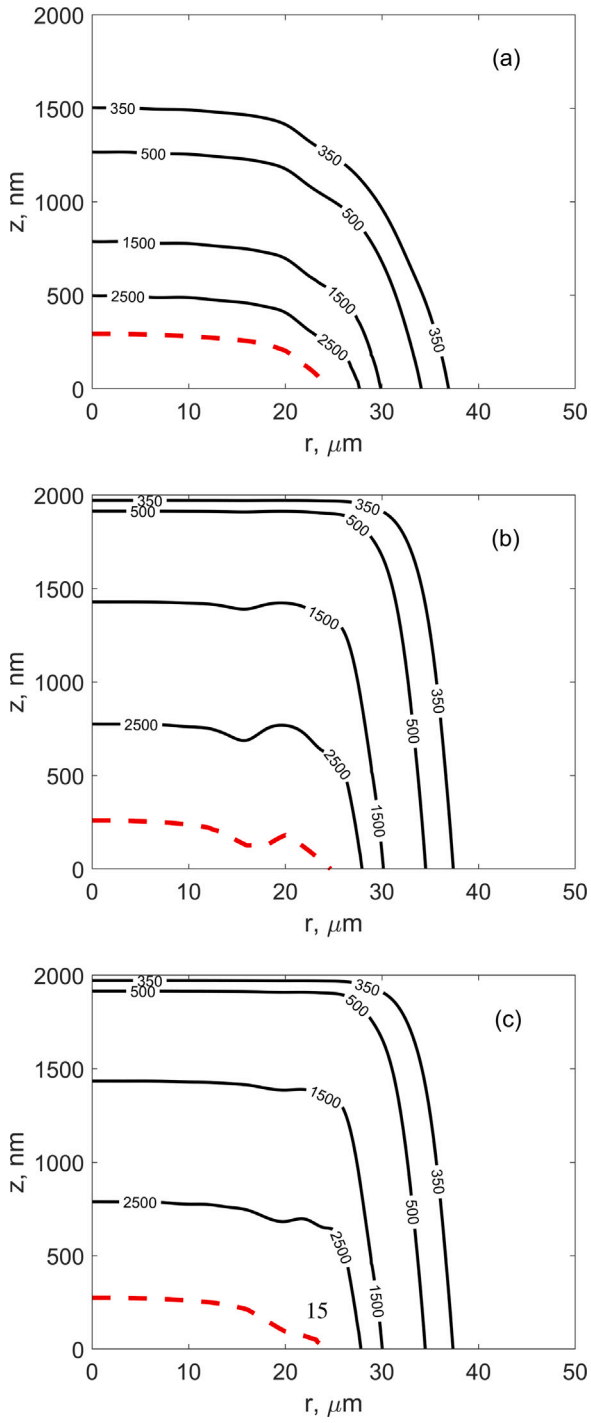

Fig. 7. Temperature contour-plots (black solid lines) and crater profiles (red dashed line). Single pulse at $t = 100$ ps (a), burst of pulses from 20/80 beamsplitter at $t = 2100$ ps (b) and burst of pulses from 40/60 beamsplitter at $t = 2100$ ps (c). $\phi_0 = 16$ J/cm^2.

shown in Fig. 7. The crater's volume was calculated as the volume of the paraboloid: $V = \pi(D/2)^2 h/2$, where D is the crater's diameter and h is the depth. The dependence dV/dE on the input fluence is presented in Fig. 8. Here, the numerical (Fig. 8a) and experimental data (Fig. 8b) are presented. As we can see, the bursts (blue and green lines, scatters) are less effective than the single pulses (red line, circles).

As it was discussed in Experiment Section, plasma shielding gives rise to particles cloud formation after the first pulse and to this reason we keep the position of the next pulse at $z = 0$, see source equation (6). The factor $\exp(-z/\delta)$ reduces the source exponentially and it vanishes at penetration depth $\delta = 18.2$ nm. The crater depth is much larger than this value and it is predefined mainly by the first pulse of the burst. As a result, in this configuration, the pulse bursts are less effective than the single pulse that accumulates all the energy of the corresponding burst.

4. Conclusions

The specific removal rate for steel and copper for single pulses and pulse bursts with different energy distribution within the burst as a function of the fluence was investigated. It was found that in general bursts lead to significantly lower specific removal rates for steel and copper samples compared to grooves ablated with single pulses. By using intraburst pulse energy distribution ratio 1:3.2:0.64:0.128:... a higher specific removal can be achieved compared to the case when the intraburst energy distribution ratio is 1:0.9:0.36:0.144:... . The highest efficiency using 1:3.2:0.64:0.128:... sequence and <2 J/cm^2 energy density was obtained, therefore for steel the removal rate was 15% and for copper only 5% lower compared to grooves ablated with the single pulses. Based on the literature a model of the ablation process was presented for steel. It also demonstrated less effectiveness of bursts compared to single pulse. In the numerical model, the pulses following the first pulse of the burst do not penetrate the material sufficiently and the crater depth remains almost unperturbed. The reason for this may be the plasma shielding that reduced the absorbed energy in the case of burst.

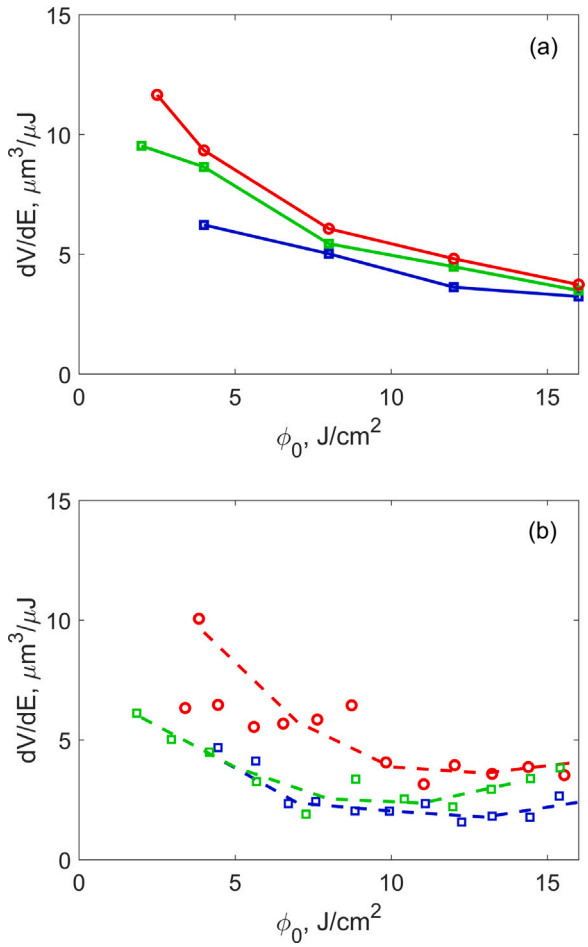

Fig. 8. Dependence of dV/dE on fluence. Single pulses (red line and circles) and bursts from 20/80 beamsplitter (blue line and scatters) as well as 40/60 beamsplitter (green and scatter). Theory (a) and experiment at scan velocity 800 mm/s (b). Lines in (b) are shown for eye-guiding. (For interpretation of the references to color in this figure legend, the reader is referred to the web version of this article.)

CRediT authorship contribution statement

Ona Balachninaitė: Conceptualization, Methodology, Investigation, Writing - original draft, Supervision. **Viktorija Tamulienė:** Conceptualization, Methodology, Formal analysis, Writing - original draft (theoretical part). **Laurynas Eičas:** Visualization, Investigation. **Virgilijus Vaičaitis:** Writing - review & editing.

Declaration of competing interest

The authors declare that they have no known competing financial interests or personal relationships that could have appeared to influence the work reported in this paper.

Acknowledgment

This research was funded by a grant (No. S-MIP-19-46) from the Research Council of Lithuania.

References

[1] Malinauskas M, Žukauskas A, Hasegawa S, Hayasaki Y, Mizeikis V, Buividas R, et al. Ultrafast laser processing of materials: from science to industry. Light: Sci Appl 2016;5(8):e16133. http://dx.doi.org/10.1038/lsa.2016.133.

[2] Mottay E, Liu X, Zhang H, Mazur E, Sanatinia R, Pfleging W. Industrial applications of ultrafast laser processing. MRS Bull 2016;41(12):984–92. http://dx.doi.org/10.1557/mrs.2016.275.

[3] Semerok A, Dutouquet C. Ultrashort double pulse laser ablation of metals. Thin Solid Films 2004;453–454:501–5. http://dx.doi.org/10.1016/j.tsf.2003.11.115.

[4] Povarnitsyn ME, Fokin VB, Levashov PR, Itina TE. Molecular dynamics simulation of subpicosecond double-pulse laser ablation of metals. Phys Rev B 2015;92(17):174104. http://dx.doi.org/10.1103/PhysRevB.92.174104.

[5] Schille J, Schneider L, Kraft S, Hartwig L, Loeschner U. Experimental study on double-pulse laser ablation of steel upon multiple parallel-polarized ultrashort-pulse irradiations. Appl Phys A 2016;122(7):644. http://dx.doi.org/10.1007/s00339-016-0169-6.

[6] Neuenschwander B, Kramer T, Lauer B, Jaeggi B. Burst mode with ps- and fs-pulses: Influence on the removal rate, surface quality, and heat accumulation. In: Roth S, Nakata Y, Neuenschwander B, Xu X, editors. Laser applications in microelectronic and optoelectronic manufacturing (LAMOM) XX. SPIE; 2015, p. 93500U. http://dx.doi.org/10.1117/12.2076455.

[7] Gaudiuso C, Kämmer H, Dreisow F, Ancona A, Tünnermann A, Nolte S. Ablation of silicon with bursts of femtosecond laser pulses. In: Heisterkamp A, Herman PR, Meunier M, Nolte S, editors. Frontiers in ultrafast optics: Biomedical, scientific, and industrial applications XVI. SPIE; 2016, 974017. http://dx.doi.org/10.1117/12.2212609.

[8] Kramer T, Neuenschwander B, Jäggi B, Remund S, Hunziker U, Zürcher J. Influence of pulse bursts on the specific removal rate for ultra-fast pulsed laser micromachining of copper. Physics Procedia 2016;83:123–34. http://dx.doi.org/10.1016/j.phpro.2016.08.024.

[9] Jaeggi B, Remund S, Streubel R, Gökce B, Barcikowski S, Neuenschwander B. Laser micromachining of metals with ultra-short pulses: Factors limiting the scale-up process. J Laser Micro/Nanoeng 2017;12(3):267–73. http://dx.doi.org/10.2961/jlmn.2017.03.0016.

[10] Kerse C, Kalaycıoğlu H, Elahi P, Çetin B, Kesim DK, Akçaalan O, et al. Ablation-cooled material removal with ultrafast bursts of pulses. Nature 2016;537(7618):84–8. http://dx.doi.org/10.1038/nature18619.

[11] Kleinert J, Lin Z, Matsumoto H. Ultrafast laser ablation of copper with ~GHz bursts. In: Neuenschwander B, Račiukaitis G, Makimura T, Grigoropoulos CP, editors. Laser applications in microelectronic and optoelectronic manufacturing (LAMOM) XXIII. SPIE; 2018, p. 126:649. http://dx.doi.org/10.1117/12.2294041.

[12] Förster DJ, Faas S, Gröninger S, Bauer F, Michalowski A, Weber R, et al. Shielding effects and re-deposition of material during processing of metals with bursts of ultra-short laser pulses. Appl Surf Sci 2018;440:926–31. http://dx.doi.org/10.1016/j.apsusc.2018.01.297.

[13] Domke M, Matylitsky V, Stroj S. Surface ablation efficiency and quality of fs lasers in single-pulse mode, fs lasers in burst mode, and ns lasers. Appl Surf Sci 2020;505:144594. http://dx.doi.org/10.1016/j.apsusc.2019.144594.

[14] Elahi P, Önder Akçaalan, Ertek C, Eken K, Ömer Ilday F, Kalaycoğlu H. High-power yb-based all-fiber laser delivering 300 fs pulses for high-speed ablation-cooled material removal. Opt Lett 2018;43(3):535–8. http://dx.doi.org/10.1364/ol.43.000535.

[15] Bonamis G, Mishchick K, Audouard E, Hönninger C, Mottay E, Lopez J, et al. High efficiency femtosecond laser ablation with gigahertz level bursts. J Laser Appl. 2019;31(2):022205. http://dx.doi.org/10.2351/1.5096087.

[16] Mishchik K, Bonamis G, Qiao J, Lopez J, Audouard E, Mottay E, et al. High-efficiency femtosecond ablation of silicon with GHz repetition rate laser source. Opt Lett 2019;44(9):2193–6. http://dx.doi.org/10.1364/ol.44.002193.

[17] Hirsiger T, Gafner M, Remund SM, Chaja MW, Urniezius A, Butkus S, et al. Machining metals and silicon with GHz bursts: Surprising tremendous reduction of the specific removal rate for surface texturing applications. In: Račiukaitis G, Molpeceres C, Narazaki A, Qiao J, editors. Laser applications in microelectronic and optoelectronic manufacturing (LAMOM) XXV. SPIE; 2020, p. 112670T. http://dx.doi.org/10.1117/12.2543948.

[18] Bonamis G, Audouard E, Hönninger C, Lopez J, Mishchik K, Mottay E, et al. Systematic study of laser ablation with GHz bursts of femtosecond pulses. Opt Express 2020;28(19):27702. http://dx.doi.org/10.1364/OE.400624.

[19] Dziatkiewicz J, Majchrzak E. Numerical analysis of laser ablation using the axisymmetric two-temperature model. In: Computer methods in mechanics (CMM2017): Proceedings of the 22nd international conference on computer methods in mechanics. Lublin, Poland; 2018, 060004. http://dx.doi.org/10.1063/1.5019065.

[20] Liu J. Simple technique for measurements of pulsed Gaussian-beam spot sizes. Opt Lett 1982;7(5):196–8. http://dx.doi.org/10.1364/ol.7.000196.

[21] Lickschat P, Metzner D, Weißmantel S. Fundamental investigations of ultrashort pulsed laser ablation on stainless steel and cemented tungsten carbide. The International Journal of Advanced Manufacturing Technology 2020;109(3-4):1167–75. http://dx.doi.org/10.1007/s00170-020-05502-8.

[22] Gamaly EG, Rode AV, Luther-Davies B, Tikhonchuk VT. Ablation of solids by femtosecond lasers: ablation mechanism and ablation thresholds for metals and dielectrics. Physics of Plasmas 2002;9(3):949–57. http://dx.doi.org/10.1063/1.1447555.

[23] König J, Nolte S, Tünnermann A. Plasma evolution during metal ablation with ultrashort laser pulses. Opt Express 2005;13(26):10597. http://dx.doi.org/10.1364/OPEX.13.010597.

[24] Ordal MA, Long LL, Bell RJ, Bell SE, Jr. RWA, Ward CA. Optical properties of the metals Al, Co, Cu, Au, Fe, Pb, Ni, Pd, Pt, Ag, Ti and W in the infrared and far infrared. Appl Opt 1983;22:1099–120.

[25] Group. Computational materials group: On-line resources. 2019, URL: http://www.faculty.virginia.edu/CompMat/electron-phonon-coupling/.